Measurement of longitudinal and transverse spin relaxation rates using the ground-state Hanle effect

N. Castagna* and A. Weis†

Département de Physique, Université de Fribourg, Chemin du Musée 3, CH-1700 Fribourg, Switzerland

(Received 28 September 2011; published 17 November 2011)

We present a theoretical and experimental study of the resonant circularly-polarized-light-induced Hanle effect in the ground state of Cs vapor atoms in a paraffin-coated cell. The effect manifests itself as a narrow resonance (centered at $B = 0$) in the dependence of the optical transmission coefficient of the vapor on the magnitude of an external magnetic field $\vec{B}$. We develop a theoretical model that yields an algebraic expression for the shape of these resonances for arbitrary field orientations and arbitrary angular momenta of the states coupled by the exciting light, provided that the light power is kept sufficiently small. An experimental procedure for assessing the range of validity of the model is given. Experiments were carried out on the laser-driven Cs D_1 transition both in longitudinal and transverse field geometries, and the observed line shapes of the corresponding bright and dark resonances give an excellent confirmation of the model predictions. The method is applied for determining the intrinsic longitudinal and transverse relaxation rates of the vector magnetization in the vapor and their dependence on light power.

DOI: 10.1103/PhysRevA.84.053421 PACS number(s): 32.80.Xx, 07.55.Ge, 32.60.+i

I. INTRODUCTION

When polarized resonance radiation is sent through a dilute atomic medium, the scattered light is, in general, polarized. In the 1920s W. Hanle observed that the degree of polarization (DOP) of the resonance fluorescence changes when the medium is exposed to a static magnetic field [1]. The effect manifests itself as a resonance structure, centered at $B = 0$, in the dependence of the DOP on B. The effect is known as magnetic depolarization of resonance fluorescence, zero-field level crossing, or just the Hanle effect (HE). Hanle studied the effect both with linear and circularly polarized light, and a detailed discussion is presented in, for example, [2,3]. The interest of the Hanle effect lies in the fact that the resonance linewidth obeys

$$\Delta B = \frac{\hbar}{\Delta m g \mu_B \tau}, \tag{1}$$

where τ is the excited state lifetime, g is the Landé factor, and μ_B is the Bohr magneton. The quantum treatment of the Hanle effect shows that it originates from the precession and relaxation of spin orientation ($\Delta m = 1$ coherences) in the excited state when excited with circularly polarized light, while under excitation with linearly polarized light it involves the precession and relaxation of spin alignment ($\Delta m = 2$ coherences). A measurement of the Hanle linewidth thus yields $g\tau$, thereby allowing a determination of the lifetime τ, when the magnetic moment $g\mu_B$ is known, or vice versa.

In the 1960s, Dupont-Roc *et al.* [4–8] observed a narrow resonance in the dependence of the intensity $I(B)$ of a resonant circularly polarized light beam on the strength of a transverse magnetic field B. Although intensity rather than polarization was measured, the authors referred to the effect as the ground-state Hanle effect (GSHE). A related effect can be observed with linearly polarized resonance radiation, in which case either changes of the intensity or the polarization are recorded. The latter effect was identified as being a linear dichroism [9,10] and became known as the nonlinear Faraday effect. It has been studied extensively, both experimentally and theoretically, in the 1980s [11].

In contrast to the (normal) HE, the various manifestations of the GSHE are nonlinear effects that involve (at least) two interactions with the light field. Optical pumping creates a spin polarization in the ground state which evolves in the magnetic field and which is probed in a subsequent interaction with the light field.

In the past decade, the GSHE with linearly polarized light has received a renewed interest [12–18] by reinterpreting it in terms of electromagnetically induced transparency or absorption (EIT or EIA), degenerate-state coherent population trapping (CPT), or λ resonances.

In this paper we report on a study of the GSHE with circularly polarized light. We derive algebraic expressions for the parameters of Hanle resonance line shapes in arbitrarily oriented magnetic fields that are valid (in the low-power limit) for arbitrary $nL_J, F \rightarrow n'L'_{J'}, F'$ electric dipole transitions. Although the GSHE with circularly polarized light has been studied by several groups in the past (see, e.g., [6,7,19–22]), we are not aware of any publication that derives explicit expressions for the line shapes. In analogy to the classical (linear) HE, the linewidths of the GSHE resonances obey relations similar to Eq. (1). We derive those relations and use them for a precision determination of the longitudinal (γ_1) and transverse (γ_2) relaxation rates of spin-orientated Cs vapor atoms in a paraffin-coated cell.

II. THEORY

A. Light absorption by spin-polarized atoms

The ground-state Hanle effect is based on spin manipulations in a vapor of polarized atoms by static magnetic fields. The effect is detected by recording field-induced changes of the optical properties of the medium. We therefore start the

*natascia.castagna@unifr.ch
†[http://physics.unifr.ch/en/page/56/]

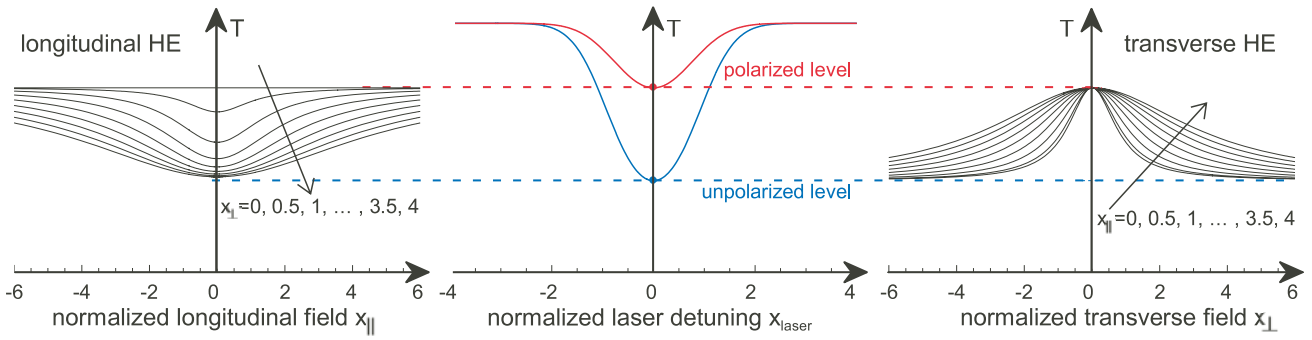

FIG. 1. (Color online) (center) Optical transmission spectrum $T(x_{\rm laser})$ in a polarized (red) and unpolarized (blue) medium. (left) Longitudinal Hanle resonances $T(x_\parallel = \omega_\parallel/\gamma_2)$ for a discrete set of transverse fields $x_\perp = \omega_\perp/\sqrt{\gamma_1\gamma_2}$. (right) Transverse Hanle resonances $T(x_\perp)$ for a discrete set of longitudinal fields $x_\parallel$. For the Hanle scans, the laser frequency is set to line center, and the field-induced change in transmission varies between the polarized and unpolarized levels.

discussion by addressing the relation between the degree of spin polarization and the light intensity transmitted by the atomic medium.

The resonant transmission T of a monochromatic laser beam tuned over an isolated atomic absorption line in an atomic vapor is given by the Lambert-Beer law:

$$T(x_{\rm laser}) \equiv \frac{I}{I_0} \equiv \frac{P}{P_0} = e^{-\kappa(x_{\rm laser})L}, \tag{2}$$

where I_0 (P_0) and I (P) are the intensity (power) of the incident and transmitted laser beam and L is the thickness of the atomic vapor. In the Doppler limit the absorption coefficient is given by

$$\kappa(x_{\rm laser}) = \kappa_0^{\rm unpol} e^{-x_{\rm laser}^2}, \tag{3}$$

where $\kappa_0^{\rm unpol} \equiv \kappa(x_{\rm laser} = 0)$ is the peak absorption coefficient of the *unpolarized* vapor, and

$$x_{\rm laser} = \frac{\omega - \omega_0}{\sqrt{2}\Gamma_D} \tag{4}$$

is the dimensionless detuning from the atomic resonance frequency ω_0, where ω is the laser frequency and Γ_D is the Doppler width. The absorption coefficient changes when the medium becomes spin polarized due to optical pumping induced by the polarized light beam.

Spin polarization is conveniently described in terms of multipole moments $m_{k,q}$ by using the irreducible tensor formalism [11]. It is well known [11,23] that an electric dipole transition is completely described by the three lowest multipole moments; viz., the total level population ($k = 0$), the spin orientation ($k = 1$), and the spin alignment ($k = 2$), that have 1, 3, and 5 independent components, respectively. More specifically, the absorption coefficient of circularly polarized light propagating along the quantization axis $\hat{z}$ depends on the longitudinal vector polarization (orientation) $\mathcal{P}_z \propto m_{1,0} \propto \langle \mathcal{F}_z \rangle$ and on the longitudinal second-rank tensor polarization (alignment) $\mathcal{A}_{zz} \propto m_{2,0} \propto \langle \mathcal{F}^2 - 3\mathcal{F}_z^2 \rangle$. In Appendix A we show that the absorption coefficient can be written as

$$\kappa_0^{\rm pol} = \kappa_0^{\rm unpol}\left(1 - \tfrac{3}{2}\mathcal{P}_z + \tfrac{3}{7}\mathcal{A}_{zz}\right). \tag{5}$$

In the present work we focus on the low-power limit, for which contributions from $\mathcal{A}_{zz}$ can be neglected, so that the polarization dependence of the absorption coefficient is given by

$$\kappa_0^{\rm pol}(\mathcal{P}_z) \approx \kappa_0^{\rm unpol}\left(1 - \tfrac{3}{2}\mathcal{P}_z\right). \tag{6}$$

Here, the longitudinal vector polarization is defined as $\mathcal{P}_z = (1/4)\sum m_F p_{m_F}$, where the p_{m_F} are the relative populations of the magnetic sublevels $\|F, m_F\rangle$. It is the manipulation of this spin polarization by static fields which is responsible for the GSHE investigated here.

Combining Eqs. (2)–(4), the laser-frequency dependence of the light power P transmitted by a medium with polarization $\mathcal{P}_z$ is given by

$$P(\mathcal{P}_z) = P_0 \exp\left[-\kappa_0^{\rm pol}(\mathcal{P}_z) L e^{-\frac{(\omega-\omega_0)^2}{2\Gamma_D^2}}\right] \tag{7}$$

$$\equiv P_0 \exp\left[-D(\mathcal{P}_z) e^{-\frac{(\omega-\omega_0)^2}{2\Gamma_D^2}}\right]. \tag{8}$$

The degree of spin polarization can be determined experimentally in the following way: We record transmission spectra when the medium is polarized ($\mathcal{P}_z = \mathcal{P}_0$) and unpolarized ($\mathcal{P}_z = 0$); see center panel of Fig. 1. Fitting the line-shape function (8) to the data yields the fit parameters $D(\mathcal{P}_0)$ and $D(0)$, respectively, which allows us to infer the spin polarization from

$$\mathcal{P}_0 = \frac{2}{3}\frac{D(0) - D(\mathcal{P}_0)}{D(0)}. \tag{9}$$

B. Ground-state Hanle effect

Ground-state Hanle resonances are recorded by locking the laser frequency to the atomic transition frequency ($x_{\rm laser} = 0$) and measuring the change of the light power P transmitted by the atomic vapor when the amplitude of a static magnetic field $\vec{B} = B_\varepsilon \hat{\varepsilon}$ of amplitude B_ε applied along $\hat{\varepsilon}$ is scanned across $B_\varepsilon = 0$.

Magnetic fields along the spin polarization vector stabilize the latter, while transverse field components make it precess and hence depolarize the medium. The principle of the Hanle effect is the interplay of polarization creation by optical pumping, polarization stabilization by longitudinal fields on one hand, and depolarization by transverse fields and intrinsic

relaxation processes on the other hand. The manifestation of the GSHE is the detection of the mentioned spin creation and evolution dynamics via a measurement of the corresponding changes in the transmitted light intensity. We note that similar effects can be observed when the polarization rather than the intensity of the transmitted light is recorded.

In what follows, we will express the field components in terms of the corresponding Larmor frequencies $\omega_\parallel = \gamma_F B_\parallel$ and $\omega_\perp = \gamma_F B_\perp$, where γ_F is the gyromagnetic ratio of the ground state ($\gamma_{F=4} = 3.498\,62$ [24] in the experiments on ^{133}Cs reported here).

We model the GSHE using the three-step approach discussed by Budker *et al*. [11]:

(1) In a first step, a longitudinal spin orientation, $\vec{\mathcal{P}}_0 = \mathcal{P}_0\hat{z}$ is created by optical pumping. Starting from a thermal distribution $p_{F,m_F} = (2F+1)^{-1}$ of the populations in the magnetic sublevels $|F,m_F\rangle$, a single cycle of absorption of a circularly polarized photon followed by reemission creates a longitudinal vector polarization (orientation) $\mathcal{P}_z$. When the light power is sufficiently low, there is no creation of higher-order (quadrupole, octupole, . . .) polarization moments by subsequent absorption and emission cycles.

(2) The second step describes the time evolution of the three components $\mathcal{P}_i$ of the vector polarization under the action of the magnetic field and relaxation. The dynamics of the vector polarization is described by the well-known Bloch equations, which yield the steady state solution (derived in Appendix B) of the longitudinal polarization

$$\frac{\mathcal{P}_z}{\mathcal{P}_0} = \frac{\omega_\parallel^2 + \gamma_2^2}{\omega_\parallel^2 + \gamma_2^2 + \frac{\gamma_2}{\gamma_1}\omega_\perp^2}, \tag{10}$$

where $\omega_\parallel = \omega_z$, $\omega_\perp^2 = \omega_x^2 + \omega_y^2$, and γ_1 and γ_2 are the longitudinal and transverse relaxation rates, respectively, of the vector polarization. $\mathcal{P}_0 = \mathcal{P}_z(\omega_\parallel = \omega_\perp = 0)$ is the polarization in the absence of fields (difficult to realize experimentally) or, equivalently, the asymptotic polarization $\mathcal{P}_z(\omega_\parallel \gg \omega_\perp)$ in a strong holding field (easy to realize experimentally). The fact that $\mathcal{P}_z$ depends only on $\omega_\parallel$ and $\omega_\perp$, independently of the orientation of the transverse field, reflects the rotational symmetry of the system of the light field.

(3) Finally, the steady state polarization $\mathcal{P}_z$ is detected via its effect of the optical absorption coefficient $\kappa(\mathcal{P}_z)$ of the medium, as discussed in Sec. II A.

We stress that this three-step approach is only valid when the laser power is sufficiently low, so that the steady state of the spin evolution is reached before the probing interaction occurs. The typical time scale for the spin dynamics (step 2) is given by γ_2^{-1}, while the time between the preparation (step 1) and probing (step 3) interactions is given by γ_p^{-1}, where $\gamma_p \propto P$ is the optical pumping rate. The three-step approach is thus valid as long as $\gamma_p < \gamma_2$.

From an experimental point of view, conditions for the validity of the model may be difficult to assess, because of the *a priori* unknown values of γ_1 and γ_2. We have used the following method that allows an empirical determination of the maximum allowed power, $P_{\max}$: The steady state spin polarization $\mathcal{P}_z$ is a nonlinear function of the laser power P_0 that can be expressed as a power series in γ_p/γ_1. The linear term in that series describes the creation of vector polarization (orientation) only. As long as $\gamma_p \ll \gamma_1$, the production of higher polarization moments is negligible. A measurement of the dependence $\mathcal{P}_z(P_0)$ therefore allows us to infer the linear regime and hence to determine $P_{\max}$.

A final remark: The three-step model has the drawback that it is only valid in the low-power limit, but has the positive aspect that it is valid for systems with arbitrary spin F, as long as the low-power limit is respected.

Equation (10) represents Lorentzian-shaped resonances (Hanle resonances) when either the longitudinal or the transverse field is scanned around zero. The amplitudes and widths of these resonances depend on the relaxation rates, and a systematic study of the resonances allows the determination of γ_1 and γ_2.

C. Line shapes in dimensionless units

Equation (10) can be rewritten in terms of dimensionless variables as

$$\frac{\mathcal{P}_z}{\mathcal{P}_0} = \frac{1 + x_\parallel^2}{1 + x_\parallel^2 + x_\perp^2}, \tag{11}$$

where

$$x_\parallel = \frac{\omega_\parallel}{\gamma_2} \quad \text{and} \quad x_\perp = \frac{\omega_\perp}{\sqrt{\gamma_1\gamma_2}}. \tag{12}$$

We speak of longitudinal (transverse) Hanle resonances when the longitudinal (transverse) field is scanned, while the transverse (longitudinal) acts as *parameter field*. The left and right parts of Fig. 1 show sets of longitudinal and transverse Hanle resonances, respectively, as given by Eq. (11) for a range of parameters fields.

D. Longitudinal Hanle effect

Longitudinal Hanle resonances are obtained by scanning the longitudinal magnetic field across $\omega_\parallel = 0$ and recording the corresponding change of the laser power $P(\omega_\parallel)$, with $\omega_\perp$ being the parameter field.

In order to extract $\mathcal{P}_z$ from the experimental signals, we first linearize Eq. (7) by taking the logarithm of the measured power $P(\omega_\parallel)$. The corresponding theoretical signal reads

$$S(\mathcal{P}_z) \equiv \ln P(\mathcal{P}_z) = \left(\ln P_0 - \kappa_0^{\text{unpol}} L\right) + \left(\kappa_0^{\text{unpol}} L\right)\mathcal{P}_z; \tag{13}$$

that is, a signal linear in $\mathcal{P}_z$. Inserting Eq. (10) into Eq. (13), one has

$$S(\omega_\parallel,\omega_\perp) \equiv \ln P(\omega_\parallel,\omega_\perp) \tag{14}$$

$$= \ln P_0 - \kappa_0^{\text{unpol}} L + \kappa_0^{\text{unpol}} L \mathcal{P}_0 \frac{\omega_\parallel^2 + \gamma_2^2}{\omega_\parallel^2 + \gamma_2^2 + \frac{\gamma_2}{\gamma_1}\omega_\perp^2}. \tag{15}$$

After some algebra, Eq. (15) can be rewritten in the form

$$S_{\text{LHE}}(\omega_\parallel;\omega_\perp) = b_\parallel - A_\parallel(\omega_\perp)\mathcal{L}_\parallel(\omega_\parallel), \tag{16}$$

which shows the resonant dependence of the longitudinal Hanle effect (LHE) on $\omega_\parallel$. In fact, Eq. (16) represents the Lorentzian

$$\mathcal{L}_\parallel(\omega_\parallel) = \frac{\gamma_\parallel^2}{\omega_\parallel^2 + \gamma_\parallel^2} \tag{17}$$

centered at $\omega_\parallel = 0$ with amplitude

$$A_\parallel(\omega_\perp) = \kappa_0^{\text{unpol}} L \mathcal{P}_0 \frac{\omega_\perp^2}{\omega_\perp^2 + \gamma_1\gamma_2} \tag{18}$$

$$= \kappa_0^{\text{unpol}} L \mathcal{P}_0 \left[1 - \frac{\gamma_1\gamma_2}{\omega_\perp^2 + \gamma_1\gamma_2}\right] \tag{19}$$

and halfwidth at half maximum

$$\gamma_\parallel(\omega_\perp) = \sqrt{\gamma_2^2 + \frac{\gamma_2}{\gamma_1}\omega_\perp^2} \tag{20}$$

that is superposed on a background

$$b_\parallel = \ln P_0 - \kappa_0^{\text{unpol}} L(1 - \mathcal{P}_0) = \ln \frac{P_0}{\kappa_0^{\text{pol}} L}. \tag{21}$$

The amplitude function $A_\parallel(\omega_\perp)$ has a Lorentzian dependence on the parameter field $\omega_\perp$, while the width function $\gamma_\parallel(\omega_\perp)$ has a hyperbolic dependence on $\omega_\perp$. The amplitude function yields the product of the relaxation rates, while the asymptotes of the width function yield their ratio. These facts form the basis of the experimental determination of the longitudinal and transverse relaxation rates.

E. Transverse Hanle effect

In the transverse Hanle effect (THE), the transverse magnetic field $\omega_\perp$ is scanned, while $\omega_\parallel$ is the parameter field. We parametrize the THE line shapes in the same way as we did for the LHE by rewriting Eq. (15) so that the scan variable $\omega_\perp$ appears explicitly, yielding

$$S_{\text{THE}}(\omega_\perp; \omega_\parallel) = b_\perp + A_\perp(\omega_\parallel)\mathcal{L}_\perp(\omega_\perp). \tag{22}$$

Equation (22) represents the Lorentzian

$$\mathcal{L}_\perp(\omega_\perp) = \frac{\gamma_\perp^2}{\omega_\perp^2 + \gamma_\perp^2} \tag{23}$$

with amplitude

$$A_\perp(\omega_\parallel) = \kappa_0^{\text{unpol}} L \mathcal{P}_0 \tag{24}$$

and halfwidth at half maximum

$$\gamma_\perp(\omega_\parallel) = \sqrt{\gamma_1\gamma_2 + \frac{\gamma_1}{\gamma_2}\omega_\parallel^2} \tag{25}$$

that is superposed on a background

$$b_\perp = \ln P_0 - \kappa_0^{\text{unpol}} L = \ln \frac{P_0}{\kappa_0^{\text{unpol}} L}. \tag{26}$$

As can be seen on the right part of Fig. 1, the transverse resonances have a constant amplitude, independent of the presence of a longitudinal field component, while the longitudinal resonances can only be observed when a transverse field is present. The latter feature is of general practical use for minimizing residual transverse fields, as discussed below.

III. EXPERIMENTS

A. Experimental apparatus

The experimental setup is shown in Fig. 2. The experiments use light from a distributed feedback (DFB) laser, whose frequency is actively stabilized to the $4 \rightarrow 3$ hyperfine transition of the cesium D_1 line using the dichroic atomic vapor laser lock (DAVLL) technique [25].

The light beam is carried by a 400 μm multimode fiber into a three-layer mu-metal shield, where the polarization of the collimated output beam is made circular by a polarizer followed by a $\lambda/4$ plate.

The Cs vapor cell is an evacuated spherical glass cell of 30 mm diameter whose inner walls are coated with a thin layer of paraffin, which efficiently reduces spin depolarization by wall collisions. In Ref. [26] we give an extensive account of the preparation and properties of our in-house paraffin-cell production. Since the cells contain no buffer gas, the atoms move on ballistic trajectories at thermal velocity, thereby efficiently averaging magnetic field inhomogeneities. This leads to a substantial line narrowing compared to buffer-gas cells. However, this is irrelevant in the present study carried out near zero magnetic field. The atomic vapor is the saturated vapor produced by a few mg of solid Cs contained in a sidearm connected by a capillary to the main cell body. The cell is kept at room temperature, and the atomic number density is 3.5×10^{16} m^{-3}, yielding an optical thickness of the unpolarized sample of $\kappa_0^{\text{unpol}} L \approx 0.60$. The (3 mm full width at half maximum, or FWHM, diameter) beam traverses the vapor cell along the z direction, and the transmitted light is detected by a photodiode followed by a current-voltage converter (FEMTO, model DLPCA-200) with an effective feedback resistor of 10^6–10^8.

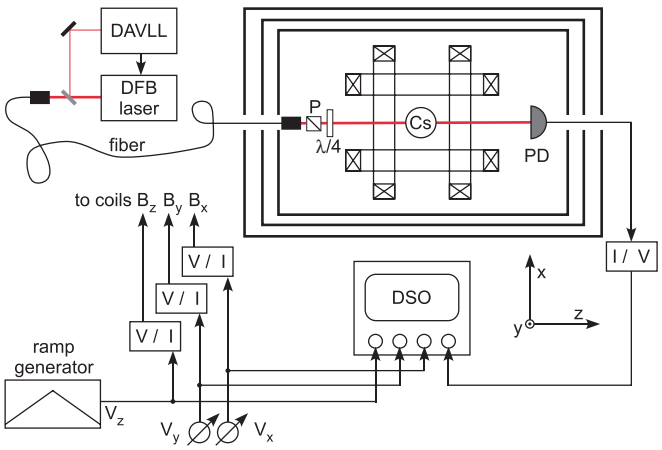

FIG. 2. (Color online) Experimental setup. The circularly polarized light of a DFB-laser stabilized on the $F = 4 \rightarrow F = 3$ hyperfine transition of the cesium D_1 line passes through a paraffin-coated vapor cell. The transmitted power is recorded by a photodiode. Three pairs of Helmholtz coils (two pairs shown) control residual fields and allow the application of a static field in an arbitrary direction. A three-layer mu-metal shield strongly suppresses external fields. P, polarizer; $\lambda/4$, quarter-wave plate; Cs, cesium vapor cell; PD, photodiode; V/I, voltage-controlled current source; I/V, transimpedance amplifier; DSO, digital storage oscilloscope.

Three mutually orthogonal pairs of Helmholtz coils allow controlling all spatial components of the magnetic field. We call the field component along $\hat{z}$ the longitudinal field, while any field component perpendicular to it is referred to as the transverse field. The three main coils are calibrated using magnetic resonances in the cell under investigation using the procedure described in Appendix C. The photodiode voltage and the three voltages controlling the components of the applied field are recorded by a four-channel digital oscilloscope. We use digital averaging by the oscilloscope in all recordings for increasing the signal-to-noise ratio.

Before starting an experimental run, we minimize the residual transverse field by using the fact, discussed in Sec. II E, that the longitudinal Hanle resonance vanishes in the absence of transverse fields. For this, we observe a Hanle resonance on the oscilloscope while scanning the longitudinal field around $B_z = 0$. By iteratively adjusting the currents generating the field components B_x and B_y, we minimize the amplitude of the Hanle resonance. After this minimization, the currents in the transverse field coils are a direct measure of the residual transverse field components. The residual longitudinal field component is obtained from the displacement of the LHE resonance $S(B_z)$ with respect to $B_z = 0$.

We note that this minimization procedure is extremely sensitive to the quality of the light polarization, and can thus also be used for optimizing the latter. When the light contains a small component of linear polarization, the Hanle resonance cannot be made to completely vanish by the field adjustment procedure described above. In that case, rotation and tilt adjustments of the quarter-wave plate are included in the iteration procedure. For recording Hanle resonances, the amplitude of the scan field ($B_\parallel$ or $B_\perp$) is scanned by a linear current ramp applied to the coils using voltage-controlled current sources driven by a voltage ramp from a function generator. The voltage ramp is recorded together with the transmitted power that contains the Hanle signal.

B. Power dependence of spin polarization

The maximal spin polarization $\mathcal{P}_0(P)$ that can be obtained depends on the laser power P.

For each laser power we have determined the degree of spin polarization as follows: We record the transmitted power $P^{\mathrm{pol}}(\omega)$ or $P^{\mathrm{unpol}}(\omega)$ by scanning the laser frequency over the 4-3 resonance under conditions in which the vapor is unpolarized ($\mathcal{P}_z = 0$) or polarized ($\mathcal{P}_z = \mathcal{P}_0$), respectively. The *polarized* transmission spectrum $P^{\mathrm{pol}}(\omega)$ is obtained by applying, during the scan, a longitudinal field B_z of $\approx 3\mu$T, which stabilizes the spin polarization created by optical pumping. The *unpolarized* transmission spectrum $P^{\mathrm{unpol}}(\omega)$ is obtained by application of transverse field B_x of $\approx 1\ \mu$T, which depolarizes the sample. Figure 3 shows a typical set of such transmission spectra.

The spectra are fit by Eq. (7) together with a linear variation of $P_0 = \alpha + \beta\omega$ that accounts for a slight change of laser power during the scan. The spin polarization $\mathcal{P}_0$ is then inferred from the fit parameters using (9). Figure 4 shows the power dependence of the spin polarization, together with a polynomial fit to guide the eye. The linear part of the fit is shown as dashed line and indicates that the creation of spin alignment is negligible for light powers below $\approx 1\ \mu$W.

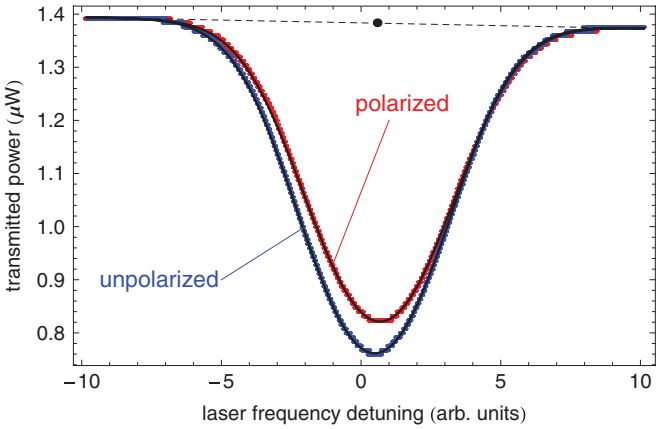

FIG. 3. (Color online) Transmission spectra of the $4 \rightarrow 3$ component of the D_1 line of spin-polarized and -unpolarized Cs vapor [dots, data; solid line, fit with combination of Eqs. (2), (3), and (6)]. The average power associated with this measurement is shown by the black dot on top. The line centers do not exactly coincide because of laser frequency drifts between the scans.

C. Recording longitudinal Hanle resonances

We recorded longitudinal Hanle resonances by scanning the longitudinal field over $B_\parallel \equiv B_z = 0$ and recording the induced changes of the transmitted light power with the laser frequency locked to the atomic transition. The scan speed is chosen to be sufficiently low (typically 10 s for a recording such as the one shown in Fig. 5) so that the spin evolution can follow the changing field adiabatically, thus avoiding resonance distortions. We repeat this scan for typically 25 different values of the parameter field $B_\perp \equiv B_x$. Figure 5 shows a typical subset of such curves, linearized by taking the logarithm of the voltage representing the light power, as discussed in Sec. II D, together with curve fits (Lorentzians on a constant background) that represent Eq. (16).

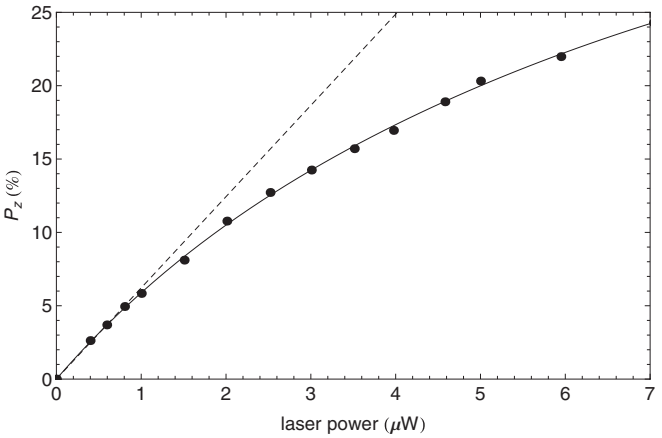

FIG. 4. Dependence of the spin polarization $\mathcal{P}_0$ on the laser power. Dots, experimental points; solid line, polynomial fit; dashed line, linear part of the polynomial fit.

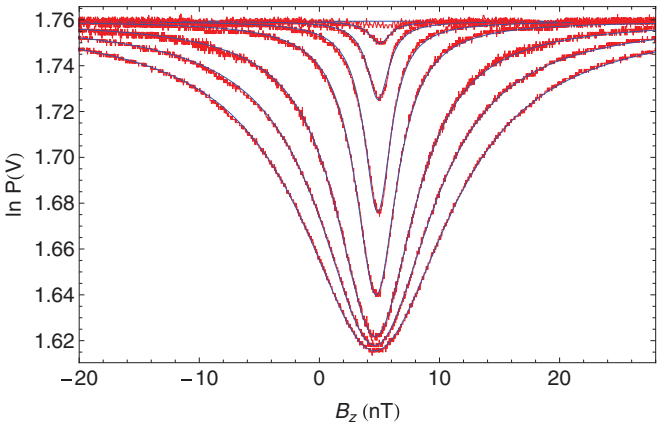

FIG. 5. (Color online) Subset of experimental LHE resonances (recorded at $P_0 = 1.6\ \mu$W) for applied transverse fields B_x of −4.2, −4.5, −4.9, −5.5, −6.6, −8.5, −10.4, and −12.3 nT (in order of increasing resonance amplitude). Data are in red and Lorentzian fits are in blue.

The residual longitudinal field in the resonances of Fig. 5 showed a slight drift during the measurements. Their average value is $\delta B_z = 3.6(1.4)$ nT. Similar values and uncertainties which reflect the residual field stability over the typically duration (2 hours) of a run are also found for the residual fields δB_x and δB_y. The background (asymptotic values of the spectra in Fig. 5) of the raw data showed variations of ≈3% over the whole range of measurements. These fluctuations are presumably due to slight fluctuations of the (unstabilized) laser power. These variations were subtracted to make all backgrounds overlap in Fig. 5.

D. Determination of relaxation rates

Each Lorentzian fit yields the amplitude $A_z(\omega_x)$ and the halfwidth at half maximum, $\gamma_z(\omega_x)$, of the Hanle curve. Figures 6 and 7 show the dependence of the amplitudes and the widths of the resonances from Fig. 5 on the applied transverse parameter field B_x.

These dependencies are fit by Eqs. (19) and (20), respectively. Taking the presence of unknown residual transverse

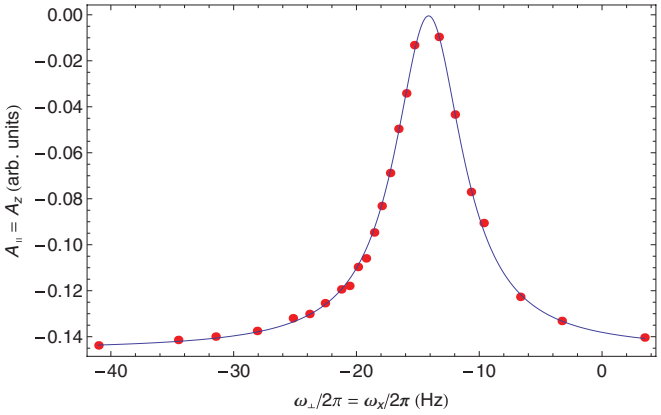

FIG. 6. (Color online) Amplitudes of the LHE resonances from Fig. 5 (dots) together with fit (solid line) according to Eq. (29). Statistical error bars (2σ) are on the order of the dot size.

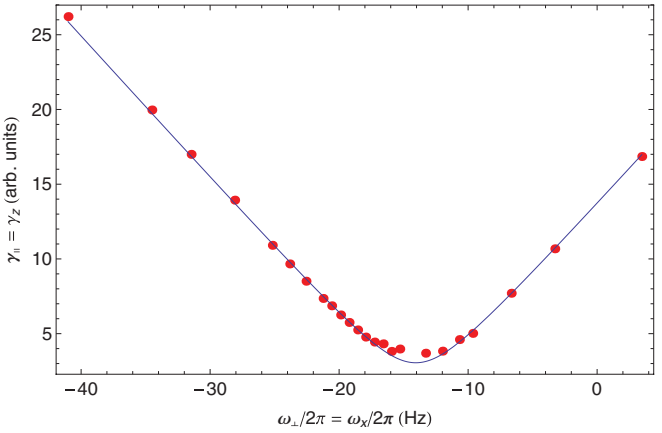

FIG. 7. (Color online) Halfwidths at half maximum of the LHE resonances from Fig. 5 (dots) together with fit (solid line) according to Eq. (30). Statistical error bars (2σ) are on the order of the dot size.

field components $\delta\omega_x$, $\delta\omega_y$ into account, the longitudinal amplitude function and the longitudinal linewidth function read

$$A_\parallel(\omega_x) = \kappa_0^{\text{unpol}} L\mathcal{P}_0 \left[1 - \frac{\gamma_1\gamma_2}{(\omega_x + \delta\omega_x)^2 + \delta\omega_y^2 + \gamma_1\gamma_2}\right] \tag{27}$$

and

$$\gamma_\parallel(\omega_x) = \sqrt{\frac{\gamma_2}{\gamma_1}(\omega_x + \delta\omega_x)^2 + \gamma_2^2 + \frac{\gamma_2}{\gamma_1}\delta\omega_y^2}, \tag{28}$$

respectively. The fit of the Lorentzian dependence (27) to the data of Fig. 6 by the function

$$A_\parallel^{\text{fit}}(\omega_x) = p_1\left[1 - \frac{p_2}{(\omega_x + p_3)^2 + p_4^2}\right] \tag{29}$$

avoids possible correlations between $\gamma_1\gamma_2$ and $\delta\omega_y$ and yields the product $p_2 = \gamma_1\gamma_2$ of the relaxation rates.

In a similar way, we avoid parameter correlations in the fitting of the linewidth function by using

$$\gamma_\parallel^{\text{fit}}(\omega_x) = \sqrt{p_1(\omega_x + p_2)^2 + p_3^2}, \tag{30}$$

which yields the ratio $p_1 = \gamma_2/\gamma_1$ that represent the slope of asymptotes to the hyperbola of (28). It is then straightforward to infer the individual values of γ_1 and γ_2 from their ratio and product.

E. Recording transverse Hanle resonances

We recorded transverse Hanle resonances by scanning the transverse field over $B_\perp \equiv B_x = 0$ and recording the induced changes of the transmitted light power with the laser frequency locked to the atomic transition. We repeat this scan for various (typically 25) values of the parameter field $B_\parallel \equiv B_z$. Figure 8 shows a set of such curves, linearized by taking the logarithm of the voltage representing the light power as discussed in Sec. II E, together with fit curves (Lorentzians on constant background) reflecting Eq. (22).

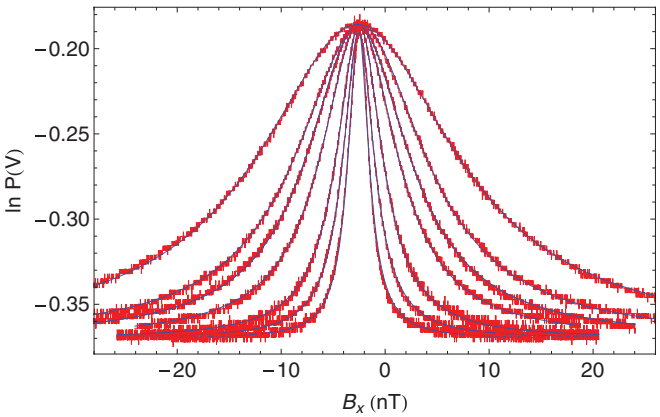

FIG. 8. (Color online) Subset of experimental THE resonances (recorded at $P_0 = 2.3\ \mu$W) for applied longitudinal fields B_z of 3.9, 2.3, 0.6, 7.9, −1.1, −3.9, and 13 nT (in order of increasing resonance width). Data are in red and Lorentzian fits are in blue. Error bars represent 2σ.

F. Determination of relaxation rates

Each Lorentzian fit yields the amplitude $A_x(\omega_z)$ and the halfwidth at half maximum $\gamma_x(\omega_z)$ of the Hanle curve. However, extraction of the relaxation rates from the transverse Hanle data is less straightforward than in the case of the longitudinal Hanle data.

The linewidth function, shown in Fig. 9, presents no problem and can be fit by (25), reexpressed in terms of the applied field and residual field components

$$\gamma_\perp(\omega_z) = \sqrt{\gamma_1\gamma_2 + \delta\omega_y^2 + \frac{\gamma_1}{\gamma_2}(\omega_z + \delta\omega_z)^2}. \tag{31}$$

Because of the correlation between $\gamma_1\gamma_2$ and $\delta\omega_y^2$, the fit permits only the extraction of the ratio γ_1/γ_2 of the relaxation rates.

The amplitude function is more problematic. Although it seems at first glance that the resonances of Fig. 8 demonstrate the independence of their amplitudes from the value of the longitudinal parameter field as predicted by theory [Eq. (24)], a plot of the amplitude fits (Fig. 10) shows that the amplitudes

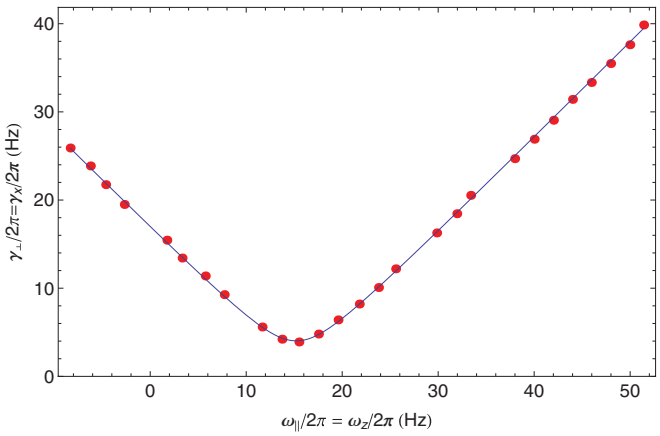

FIG. 9. (Color online) Halfwidths at half maximum of the THE resonances from Fig. 8 (dots) together with fit (solid line) according to Eq. (31). Statistical error bars (2σ) are on the order of the dot size.

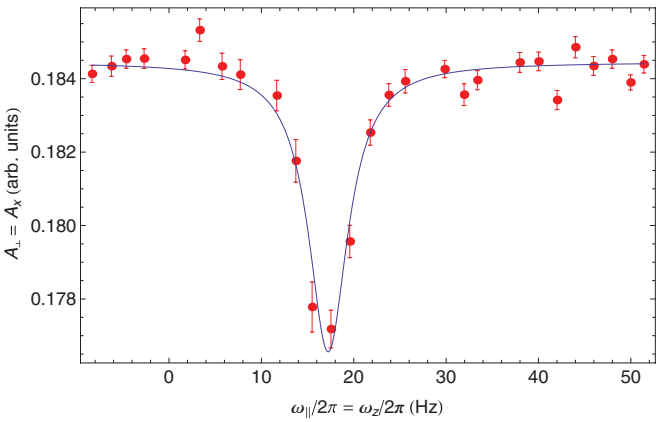

FIG. 10. (Color online) Amplitudes of LHE resonances from Fig. 8 (dots) together with fit (solid line) according to Eq. (32).

have a small longitudinal-field dependence of a few percent. The origin of this feature is the presence of a residual transverse field component $\delta\omega_y$, as can be seen by including that component in Eq. (24):

$$A_\perp(\omega_z) = \kappa_0^{\text{unpol}} L\mathcal{P}_0 \left[1 - \frac{\delta\omega_y^2}{\frac{\gamma_1}{\gamma_2}(\omega_z + \delta\omega_z)^2 + \gamma_1\gamma_2 + \delta\omega_y^2}\right]. \tag{32}$$

This expression reduces to (24) only when $\delta\omega_y = 0$. The poor signal-to-noise ratio of the data in Eq. (8) and parameter correlations in Eq. (32) do not allow their use for extracting information on the relaxation rates. Nonetheless, a fit of the data with (32) permits us to obtain the asymptotic value $A_\perp^\infty \equiv A_\perp(\omega_z \to \infty) = \kappa_0^{\text{unpol}} L\mathcal{P}_0$ with a good accuracy.

For the extraction of both γ_1 and γ_2 we found it useful to introduce the combination

$$G_\perp(\omega_z) \equiv \frac{A_\perp(\omega_z)\gamma_\perp^2(\omega_z)}{\kappa_0^{\text{unpol}} L\mathcal{P}_0}, \tag{33}$$

in which the quantities in the numerator are the fit parameters of the individual Hanle resonances, and where the denominator is the value obtained from the fit of $A_\perp(\omega_z)$, outlined above.

Combining (31) and (32), one sees that the theoretical expression for the $G_\perp$ function is given by the parabolic dependence

$$G_\perp(\omega_z) = \frac{\gamma_1}{\gamma_2}(\omega_z + \delta\omega_z)^2 + \gamma_1\gamma_2, \tag{34}$$

the fitting of which to the $G_\perp$ data yields the product and ratio, and hence the individual values of the relaxation rates (Fig. 11).

G. Intrinsic relaxation rates

We repeated the measurements described above for a range of laser power levels. The resulting linewidths are shown in Fig. 12.

At low powers both γ_1 and γ_2 depend in a linear manner on the laser power P_0, while their power broadening becomes nonlinear for powers above $\approx 1\ \mu$W, as expected from the discussion in Sec. III B. We have fit the power-broadening data by (phenomenological) weighted second-order polynomials,

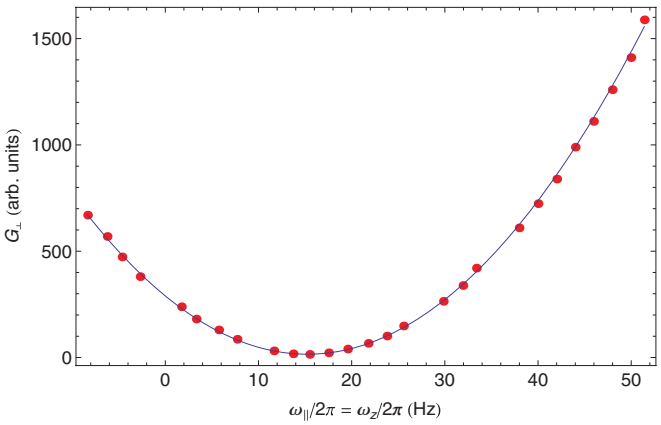

FIG. 11. (Color online) $G_\perp$ data calculated from the fit parameters of the transverse Hanle resonances according to (33), together with fit using the function defined by (34).

whose intercepts yield the intrinsic relaxation rates

$$\frac{\gamma_{10}}{2\pi} \equiv \frac{\gamma_1(P_0 = 0)}{2\pi} = 1.8(1)\ \text{Hz}, \tag{35}$$

$$\frac{\gamma_{20}}{2\pi} \equiv \frac{\gamma_2(P_0 = 0)}{2\pi} = 2.1(1)\ \text{Hz}, \tag{36}$$

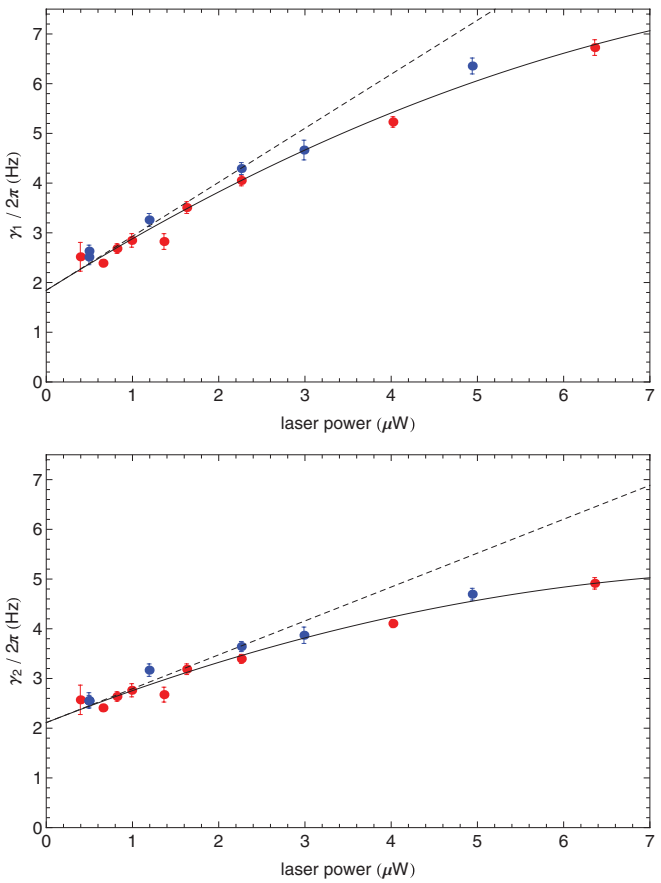

FIG. 12. (Color online) Dependence of the longitudinal and transverse relaxation rates on laser power. Data from the LHE run in red; data from the THE run in blue. The solid line represents a weighted fit of a second-order polynomial to all data points. The dashed line represents the constant and linear part of that fit.

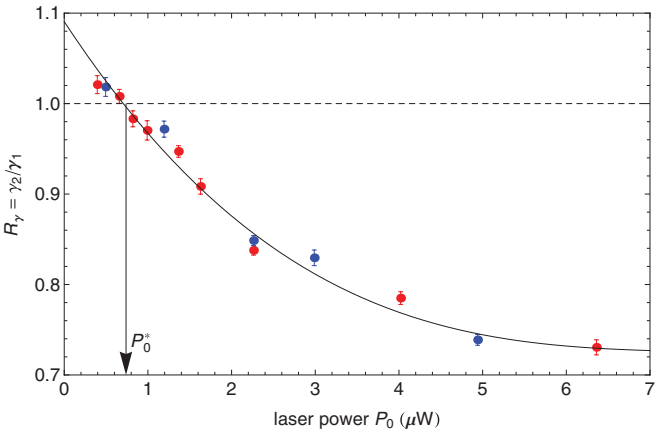

FIG. 13. (Color online) Dependence of the ratio of relaxation rates on laser power. Data from the LHE run in red; data from the THE run in blue. The solid line is a Lorentzian fit (see text). P_0^* denotes the power for which $\gamma_1 = \gamma_2$.

and linear power broadening rates

$$\frac{1}{2\pi}\frac{d\gamma_1}{dP_0} = 1.1(1)\ \frac{\text{Hz}}{\mu W}, \tag{37}$$

$$\frac{1}{2\pi}\frac{d\gamma_2}{dP_0} = 0.68(9)\ \frac{\text{Hz}}{\mu W}. \tag{38}$$

We note that, at low powers, $\gamma_2 < \gamma_1$, while at large powers, $\gamma_1 > \gamma_2$. This can also be seen from a plot of the ratio $R_\gamma = \gamma_2/\gamma_1$ represented in Fig. 13, which shows that $\gamma_1 \approx \gamma_2$ for $P_0 = 0.74(5)\ \mu$W.

The solid line in Fig. 13 represents a weighted third-order polynomial, which is meant to guide the eye since we have no algebraic theoretical prediction for the power dependence of R_γ. The ratio of relaxation rates extrapolates to $R_\gamma(P_0 \to 0) = 1.09(2)$.

The T_1 ($=\gamma_1^{-1}$) time in paraffin-coated cells is believed to be mainly due to losses of atoms into the (uncoated) sidearm of the cell that connect the cell volume to the reservoir containing the solid Cs droplet (reservoir effect) and to imperfections in the coating layer. Following the arguments and equations presented in Ref. [26] we can estimate the effective loss surface of the inner cell wall to be on the order of 4 mm^2 ($\approx$0.1% of the total inner-cell surface), which is 10 times larger than the cross section of the capillary leading to the reservoir.

Two years ago we measured the intrinsic relaxation rates in the same cell using the technique of optically detected magnetic resonance described in Ref. [26]. That previous measurements yielded larger values of the intrinsic relaxation rates of $\gamma_{10}/(2\pi) = 2.3(2)$ Hz and $\gamma_{20}/(2\pi) = 3.5(1)$ Hz. The T_1 time determined by optically detected magnetic resonance (ODMR) is compatible with its present determination (35), while the T_2 time determined by the Hanle technique time is 1.7(1) times larger than the one obtained in the ODMR study. A possible explanation might be field inhomogeneities or field instabilities (due to current source fluctuations) in the ODMR experiment to which the GSHE technique is not sensitive since it uses $B \approx 0$.

IV. CONCLUSION AND OUTLOOK

We have derived an algebraic expression for the shape of ground-state Hanle resonances. The expression is valid for magnetic fields of arbitrary orientation and for transitions between states with arbitrary angular momenta, as long as the laser power is kept sufficiently low. We have described an experimental method for assessing the range of light powers that ensure the validity of the model predictions. Our detailed study of the amplitudes and widths of longitudinal and transverse Hanle resonances are fully compatible with the model predictions. We applied the method to determine the intrinsic longitudinal and transverse relaxation rates of spin-oriented atoms in a paraffin-coated cesium vapor cell by extrapolating the light-power dependence of the rates to zero power. The relaxation rates are obtained with an accuracy of ≈5%.

The method described here complements our standard procedure for assessing the quality of in-house-produced coated cells [26]. The latter method is based on optically detected magnetic resonances and the determination of intrinsic relaxation rates involves the extrapolation of both the rf power and the laser power to zero.

We have also derived algebraic expressions for the GSHE excited with *linearly* polarized light. In that case the spin polarization of the ground state is determined by the second-rank atomic alignment tensor $\mathcal{A}_q^{(2)}$, whose relaxation is described by three independent relaxation rates, $\gamma_{|q|=0}$, $\gamma_{|q|=1}$, and $\gamma_{|q|=2}$. We are currently making detailed measurements of the characteristics of the GSHE with linear light polarization. The results will be reported in a forthcoming presentation.

ACKNOWLEDGMENTS

We acknowledge financial support by the Swiss National Science Foundation Sinergia Grant No. CRSII2-130414-1.

APPENDIX A: RESONANT LIGHT ABSORPTION BY SPIN-POLARIZED ATOMS

The absorption coefficient for σ_+-polarized light on the $|6S_{1/2},F=4,m_F\rangle \rightarrow |6P_{1/2},F=3,m_F+1\rangle$ sublevel transition is proportional to the square of the transition dipole matrix element, itself proportional to the square of the corresponding $3j$ symbol

$$\kappa_{4,m_F\rightarrow 3,m_F+1} = K \begin{pmatrix} 3 & 1 & 4 \\ -m_F-1 & 1 & m_F \end{pmatrix}^2 \tag{A1}$$

$$= \frac{K}{504}(m_F-3)(m_F-4). \tag{A2}$$

In Eq. (A2) we have assembled all common proportionality factors in the constant K. Note that the algebraic expression of the $3j$ symbol reflects well the fact that the $m_F=3,4$ sublevels are dark states for σ_+ light. The total absorption coefficient is given by the weighted sum of (A2):

$$\kappa = \sum_{m_F=-4}^{4} p_{m_F}\kappa_{4,m_F\rightarrow 3,m_F+1}, \tag{A3}$$

where the p_{m_F} are the relative, $\sum p_{m_F}=1$, sublevel populations of the $F=4$ ground state.

Inserting the thermal populations $p_{m_F}=(2F+1)^{-1}=1/9$, one obtains the unpolarized absorption coefficient

$$\kappa^{\text{unpol}} = \frac{K}{9}\sum_{m_F=-4}^{4}\kappa_{4,m_F\rightarrow 3,m_F+1} = \frac{K}{27}. \tag{A4}$$

The polarized absorption coefficient is obtained by inserting Eq. (A2) into Eq. (A3), yielding

$$\kappa^{\text{pol}} = \frac{K}{504}\left(12\sum p_{m_F} - 7\sum m_F p_{m_F} + \sum m_F^2 p_{m_F}\right). \tag{A5}$$

We define the longitudinal orientation $\mathcal{P}_z$ and the longitudinal alignment $\mathcal{A}_{zz}$ as

$$\mathcal{P}_z \equiv \frac{1}{4}\sum m_F p_{m_F} \tag{A6}$$

and

$$\mathcal{A}_{zz} \equiv \frac{1}{24}\sum\left[3m_F^2 - F(F+1)\right]p_{m_F} \tag{A7}$$

$$= \frac{1}{24}\sum\left(3m_F^2-20\right)p_{m_F}, \tag{A8}$$

normalized such that $\mathcal{P}_z$ and $\mathcal{A}_{zz}$ have unit value when the medium is in the stretched state defined by $p_{m_F}=\delta_{m_F,4}$. Introducing Eq. (A6) and (A8) into Eq. (A5), we obtain

$$\kappa^{\text{pol}} = K\left(\tfrac{1}{27} - \tfrac{1}{18}\mathcal{P}_z + \tfrac{1}{63}\mathcal{A}_{zz}\right) \tag{A9}$$

$$= \kappa^{\text{unpol}}\left(1 - \tfrac{3}{2}\mathcal{P}_z + \tfrac{3}{7}\mathcal{A}_{zz}\right), \tag{A10}$$

where we have used (A4).

APPENDIX B: STEADY STATE POLARIZATION

The evolution of the vector polarization $\vec{\mathcal{P}}$ in a static field $\vec{B}$ with corresponding Larmor frequencies $\vec{\omega}=(\omega_x,\omega_y,\omega_z)$ is described by the Bloch equations

$$\dot{\vec{\mathcal{P}}} = \vec{\omega}\times\vec{\mathcal{P}} - \vec{\mathcal{P}}_{\text{relax}}, \tag{B1}$$

whose components read

$$\begin{pmatrix}\dot{\mathcal{P}}_x\\ \dot{\mathcal{P}}_y\\ \dot{\mathcal{P}}_z\end{pmatrix} = \begin{pmatrix}\omega_x\\ \omega_y\\ \omega_z\end{pmatrix}\times\begin{pmatrix}\mathcal{P}_x\\ \mathcal{P}_y\\ \mathcal{P}_z\end{pmatrix} - \begin{pmatrix}\gamma_2\mathcal{P}_x\\ \gamma_2\mathcal{P}_y\\ \gamma_1(\mathcal{P}_z-\mathcal{P}_0)\end{pmatrix}, \tag{B2}$$

where $\mathcal{P}_0$ is the spin polarization created by optical pumping.

The steady state solutions $\dot{\vec{\mathcal{P}}}=0$ of Eq. (B2) are readily obtained and yield

$$\mathcal{P}_z = \mathcal{P}_0\frac{\omega_z^2+\gamma_2^2}{\omega_z^2+\gamma_2^2+\frac{\gamma_2}{\gamma_1}\left(\omega_x^2+\omega_y^2\right)}, \tag{B3}$$

which is equivalent to Eq. (10).

It is interesting to note that, in the case $\gamma_1=\gamma_2\equiv\gamma$, Eq. (B3) can be written as

$$\frac{\mathcal{P}_z}{\mathcal{P}_0} = \frac{1+\beta_z^2}{1+\beta^2}, \tag{B4}$$

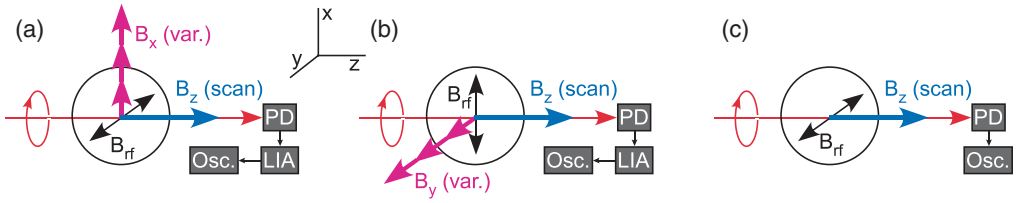

FIG. 14. (Color online) Field geometries for calibrating the B_x coils (a), the B_y coils (b), and the B_z coils (c). PD, photodiode; LIA, lock-in amplifier; Osc., oscilloscope.

where $\beta_i = \omega_i/\gamma$ and $\beta = |\vec{\beta}|$. This equation can be expressed in the compact form

$$\frac{\mathcal{P}_z}{\mathcal{P}_0} = \sum_{q=-1}^{1} \frac{\left|C_1^q(\theta,\varphi)\right|^2}{1+q^2\beta^2}, \tag{B5}$$

where the C_{1q} are the spherical components of the unit vector

$$C_1^q(\theta,\varphi) = \sqrt{\frac{4\pi}{3}}\,Y_1^q(\theta,\varphi). \tag{B6}$$

APPENDIX C: COIL CALIBRATION

We calibrate the three coils (Helmholtz coils) using optically detected magnetic resonance (ODMR) signals with the cell in the same position as for the Hanle measurements (procedure similar to the one described in Ref. [27]).

1. Calibration of B_z coil

We use the M_z magnetometer technique for calibrating the coils producing the field component B_z [Fig. 14(c)]. A weak magnetic field $\vec{B}_{\rm rf}$ oscillating at the frequency $\nu_{\rm rf}$ of several hundred Hz is applied in the y direction. This field drives magnetic resonance transitions when the condition

$$\omega_{\rm rf} = 2\pi\,\nu_{\rm rf} = \gamma_F|\vec{B}_{\rm tot}| = \sqrt{B_x^2 + B_y^2 + B_z^2} \tag{C1}$$

is met. Before the calibration measurements we minimize at best the residual static field components δB_x and δB_y using the technique described in the main text. Since we cannot assure that all residual field components vanish, we have to express Eq. (C1) as

$$\nu_{\rm rf} = \frac{\gamma_F}{2\pi}|\vec{B}_{\rm tot}| = \sqrt{\delta B_x^2 + \delta B_y^2 + (\varepsilon_z V_z + \delta B_z)^2}, \tag{C2}$$

where V_z is the voltage controlling the current source that drives the B_z coil and ε_z ($[\varepsilon_z] = $ Hz/mV) is the sought calibration constant.

We record variations of the transmitted light intensity when the longitudinal field component ω_z is scanned around $\omega_{\rm rf}$. We measured a set of such spectra for various discrete values of $\nu_{\rm rf}$ in the range between 400 and 1700 Hz. Each spectrum was fit by a Lorentzian on a flat background and the voltage V_z^* of the resonance position was determined by a Lorentzian fit. A fit of (C2) to the data thus obtained (Fig. 15) determines the calibration constant ε_z.

2. Calibration of B_x and B_y coils

For the calibration of the transverse field coils, we applied the M_x-magnetometer technique that relies on the fact that the transmitted light intensity is modulated at the frequency $\nu_{\rm rf}$ when the magnetic field is neither parallel nor perpendicular to the propagation direction $\hat{k}$ of the light. The amplitude of the intensity modulation is extracted by a lock-in amplifier tuned to $\nu_{\rm rf}$. For calibrating the B_x coil we had the weak field oscillating in the y direction at a fixed frequency of $\nu_{\rm rf} =$ 864.5 Hz [Fig. 14(a)]. We then applied a set of constant fields B_x and scanned B_z over the (single) magnetic resonance line. From a Lorentzian fit to the line we determined the voltage V_z^* and hence the frequency $\nu_z^* = \gamma_F\varepsilon_z V_z^*/(2\pi)$ of the resonance line center. According to (C1), the relation $\nu_z^*(V_x)$ reads

$$\nu_z^* = -\delta\nu_z + \sqrt{\nu_{\rm rf}^2 - \delta\nu_y^2 - (\varepsilon_x V_x + \delta\nu_x)^2}, \tag{C3}$$

which allows us to infer the calibration constant ε_x from a fit (Fig. 16).

The B_y coil is calibrated in the same manner [Fig. 14(b)].

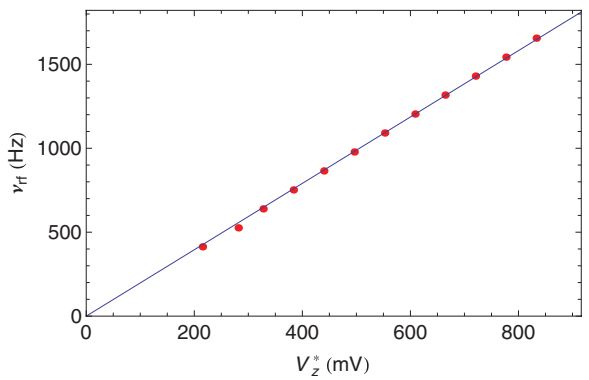

FIG. 15. (Color online) Calibration of B_z coil (see text).

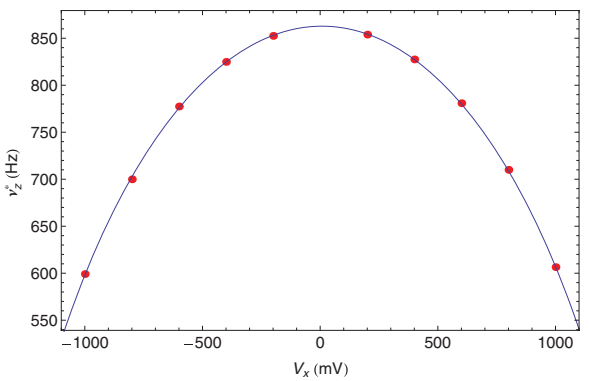

FIG. 16. (Color online) Calibration of B_x coil (see text).

[1] W. Hanle, Z. Phys. **30**, 93 (1924).
[2] A. C. G. Mitchell and M. W. Zemansky, *Resonance Radiation and Excited Atoms* (Cambridge University Press, London, 1971).
[3] A. Corney, *Atomic and Laser Spectroscopy* (Oxford University Press, Oxford, 1987).
[4] J. Dupont-Roc, S. Haroche, and C. Cohen-Tannoudji, Phys. Lett. A **28**, 638 (1969).
[5] J. C. Lehmann and C. Cohen-Tannoudji, C. R. Acad. Sc. Paris **258**, 4463 (1964).
[6] C. Cohen-Tannoudji, J. Dupont-Roc, S. Haroche, and F. Laloë, Rev. Phys. Appl. **5**, 102 (1970).
[7] M. Bouchiat, J. Brossel, C. Cohen-Tannoudji, J. Dupont-Roc, S. Haroche, A. Kastler, and J. C. Lehmann, US Patent No. 3,629,697 (21 December 1971).
[8] R. E. Slocum, Phys. Rev. Lett. **29**, 1642 (1972).
[9] A. Weis and S. I. Karnorsky, J. Opt. Soc. Am. B **10**, 716 (1992).
[10] S. I. Kanorsky, A. Weis, J. Wurster, and T. W. Hänsch, Phys. Rev. A **47**, 1220 (1993).
[11] D. Budker, W. Gawlik, D. F. Kimball, S. M. Rochester, V. V. Yashchuk, and A. Weis, Rev. Mod. Phys. **74**, 1153 (2002).
[12] F. Renzoni, W. Maichen, L. Windholz, and E. Arimondo, Phys. Rev. A **55**, 3710 (1997).
[13] M. Auzinsh, R. Ferber, F. Gahbauer, A. Jarmola, and L. Kalvans, Phys. Rev. A **78**, 013417 (2008).
[14] M. Auzinsh, R. Ferber, F. Gahbauer, A. Jarmola, and L. Kalvans, Phys. Rev. A **79**, 053404 (2009).
[15] G. Théobald, N. Dimarcq, V. Giordano, and P. Cérez, Opt. Commun. **71**, 256 (1989).
[16] E. Alipieva, S. V. Gateva, and E. Taskova, IEEE Trans. Circuit Syst. **54**, 738 (2005).
[17] Y. Dancheva, G. Alzetta, S. Carteleva, M. Taslakov, and C. Andreeva, Opt. Commun. **178**, 103 (2000).
[18] M. M. Mijailović, J. Dimitrijević, A. J. Krmpot, Z. D. Grujić, B. M. Panić, D. Arsenović, D. V. Pantelić, and B. M. Jelenković, Opt. Express **15**, 1328 (2007).
[19] S. Gozzini, S. Cartaleva, A. Lucchesini, C. Marinelli, L. Marmugi, D. Slavov, and T. Karaulanov, Eur. Phys. J. D **53**, 153 (2009).
[20] A. Huss, R. Lammegger, L. Windholz, E. Alipieva, S. Gateva, L. Petrov, E. Taskova, and G. Todorovov, J. Opt. Soc. Am. B **23**, 1729 (2006).
[21] Ch. Andreeva, S. Cartaleva, Y. Dancheva, V. Biancalana, A. Burchianti, C. Marinelli, E. Mariotti, L. Moi, and K. Nasyrov, Phys. Rev. A **66**, 012502 (2002).
[22] A. Villardi, D. Tabarelli, L. Botti, A. Bertoldi, and L. Ricci, J. Phys. B **42**, (2009).
[23] W. Happer, Rev. Mod. Phys. **44**, 169 (1972).
[24] J. Vanier and C. Audoin, *The Quantum Physics of Atomic Frequency Standards*, Adam Hilger imprint (IOP Publishing, Ltd., Bristol and Philadelphia, 1989).
[25] K. L. Corwin, Z. T. Lu, C. F. Hand, R. J. Epstain, and C. E. Wieman, Appl. Opt. **37**, 3295 (1998).
[26] N. Castagna, G. Bison, G. Di Domenico, A. Hofer, P. Knowles, C. Macchione, H. Saudan, and A. Weis, Appl. Phys. B **96**, 763 (2009).
[27] M. Arndt, S. I. Kanorsky, A. Weis, and T. W. Hänsch, Phys. Rev. Lett. **74**, 1359 (1995).